Nanoscale

Graphene Coated Nanoporous Nickel towards Metal-Catalyzed Oxygen Evolution Reaction

Journal:	*Nanoscale*
Manuscript ID	NR-ART-04-2021-002074.R1
Article Type:	Paper
Date Submitted by the Author:	15-May-2021
Complete List of Authors:	Qiu, Hua-Jun; Harbin Institute of Technology, Johnson, Isaac; Johns Hopkins University Chen, Luyang; East China University of Science and Technology, Cong, Weitao; East China Normal University Ito, Yoshikazu; University of Tsukuba, Liu, Pan; WPI-AIMR, ; Shanghai Jiao Tong University, Han, Jiuhui; Tohoku University, Kateshi, Fujita; Tohoku University Hirata, Akihiko; a. WPI Advanced Institute for Materials Research, Tohoku University, Chen, Mingwei; Johns Hopkins University, Materials Science and Engineering; Tohoku University, WPI-AIMR

Graphene Coated Nanoporous Nickel towards Metal-Catalyzed Oxygen Evolution Reaction

Hua-Jun Qiu,[1†] Isaac Johnson,[2†] Luyang Chen,[3†] Weitao Cong,[4] Yoshikazu Ito,[5] Pan Liu,[6, 7] Jiuhui Han,[7] Takeshi Fujita,[7] Akihiko Hirata[7], and Mingwei Chen[2,7*]

[1]School of Materials Science and Engineering, Harbin Institute of Technology (Shenzhen), Shenzhen, 518055, China Email: qiuhuajun@hit.edu.cn

[2]Department of Materials Science and Engineering, Johns Hopkins University, Baltimore, MD 21218, USA

[3]School of Materials Science and Engineering, East China University of Science and Technology, Shanghai 200237, China

[4]Key Laboratory of Polar Materials and Devices, East China Normal University, Shanghai 200062, China

[5]Institute of Applied Physics, Graduate School of Pure and Applied Sciences, University of Tsukuba, Tsukuba 305–8573, Japan

[6]State Key Laboratory of Metal Matrix Composites, School of Materials Science and Engineering, Shanghai Jiao Tong University, Shanghai 200030, China

[7]WPI Advanced Institute for Materials Research, Tohoku University, Sendai 980-8577, Japan

*Corresponding Author: Email: mwchen@jhu.edu

† These authors contributed equally to this work.

ABSTRACT

Developing highly active electrocatalysts with low costs and long durability for oxygen evolution reactions (OER) is crucial towards the practical implementations of electrocatalytic water-splitting and rechargeable metal-air batteries. Anodized nanostructured *3d* transition metals and alloys with the formation of OER-active oxides/hydroxides are known to have high catalytic activity towards OER but suffer from poor electrical conductivity and electrochemical stability in harsh oxidation environments. Here we report that high OER activity can be achieved from metallic state of Ni which is passivated by atomically-thick graphene in a three-dimensional nanoporous architecture. As a free-standing catalytic anode, the non-oxide transition metal catalyst shows a low OER overpotential, high OER current density and long cycling lifetime in alkaline solutions, benefiting from the high electrical conductivity and low impedance resistance for charge transfer and transport. This study may pave a new way to develop high efficiency transition metal OER catalysts for a wide range of applications in renewable energy.

KEYWORDS: Graphene coating, nanoporous nickel, free-standing electrode, OER

Introduction

Oxygen evolution reactions (OERs) are the critical step in electrochemical water splitting and rechargeable metal-oxygen batteries, which often have a high overpotential and sluggish reaction kinetics[1-4]. An active electrocatalyst is necessary to reduce the reaction overpotentials and to enhance the reaction efficiency. It is known that precious metal oxides, such as RuO_2 and IrO_2[5, 6], are active OER catalysts. However, the high material costs and natural resource scarcity prevent the wide-range of practical applications of these catalysts. Recently, much efforts have been made to develop highly active, durable and low-cost alternatives[7-24]. Owing to the earth-abundant nature

and theoretically high catalytic activity, anodized *3d* transition metals, such as Ni and Ni alloys (such as NiFe, NiCo, etc), are emerging as the most promising ORE catalysts and have been used in commercial electrolysers [25-40]. To maintain high catalytic activities and electrical conductivity, Ni-based catalysts are usually prepared as thin films on conductive substrates by electrodeposition, sputtering, dip-coating, drop-coating, etc[33, 41-43]. Although significant improvements have been achieved over the past decade, the practical applications of Ni-based OER catalysts are still limited by the low catalytic activity, insufficient electric conductivity and poor stability. Thus, the development of robust OER catalytic electrodes with a high surface area, high electrical conductivity and high stability is urgent for renewable energy applications.[44]

In general, the OER catalysis of 3d transition metals originates from the formation of surface oxides/hydroxides in oxidation environments, which are catalytically active for OER.[45-47] Thus, direct anodization of nanostructured Ni and Ni-based alloys with a large effective surface area is a feasible way to produce highly active Ni hydroxide for OER applications.[48] However, the uncontrollable anodization usually results in the formation of excess Ni oxide and hydroxide that cause the quick loss of both electrical conductivity and the catalytic activity[31]. Therefore, effectively controlling the anodization of Ni based electrodes is crucial in developing high performance Ni-based OER catalysts. Recently, we developed a 3D nanoporous nickel (np-Ni) with a large effective surface area, high chemical activity and high electric conductivity[49]. Although it shows excellent performances in electrocatalysis and energy storage, the brittleness and poor electrochemical stability, similar to other nanostructured transition metals, exclude the direct use of np-Ni as a free-standing OER catalytic electrode. In this study, we report that atomic-thick graphene coating can dramatically improve the electrochemical stability of np-Ni and, different from conventional wisdom, we find that the graphene coated np-Ni (graphene@np-Ni) with almost pure metallic Ni surface shows superior catalytic activities towards OER in alkaline solutions. Although it has been noticed that a lower valence of *3d* transition metals enables lower

overpotentials of OER[50, 51], this could be the first demonstration that the metallic transition metals are OER active when chemically active nanostructured Ni is passivated by highly conductive and electrochemically stable graphene.

RESULTS AND DISCUSSION

The graphene@np-Ni was fabricated by a np-Ni based chemical vapor deposition (CVD) method[52, 53]. The morphology of the graphene@np-Ni was characterized by scanning electron microscopy (SEM). As shown in the top-view SEM image (Figure 1a), the ligament and pore size of the nanoporous composite is ~200-400 nm. The cross-sectional SEM image (Figure 1b) shows that the nanoporous structure is uniform across the entire sample with a thickness of ~30 μm. Since the graphene layer is too thin to be viewed by SEM, we characterized the formation of graphene by Raman spectroscopy (Figure 1c). The broad 2D band (2712 cm^{-1}), together with the low intensity ratio between 2D and G bands, demonstrate the formation of bi-layer and few-layer graphene on the internal surface of np-Ni, consistent with previous reports of CVD grown graphene on Ni[54, 55]. The appearance of weak D band (1348 cm^{-1}) in the Raman spectra indicates the existence of structural defects in the as-grown graphene[56, 57], which is mainly due to the high curvature gradient of the 3D nanoporous geometry[52]. The formation of a continuous graphene layer on the internal surface of np-Ni is directly approved by the complete dissolution of the np-Ni substrate in 2.0 M HCl aqueous solution. As shown in Figure 1d and Figure S1b (Supporting Information), a piece of free-standing nanoporous graphene sheet can be obtained after Ni dissolution. The nanoporous graphene shows an interconnected nanotubular-like porous structure, which fully inherits the surface morphology of Ni ligaments in np-Ni and also demonstrates that the internal surface of np-Ni is fully covered by graphene. The selected area electron diffraction pattern (inset in Figure 1d) reveals the high crystallinity of graphene. There is no detectable structural change in the free-standing graphene after the Ni dissolution as shown in the Raman

spectrum (Figure 1c), indicating that the excellent durability of the nanoporous graphene. The 3D graphene@np-Ni was further characterized by scanning transmission electron microscopy (STEM) at high magnifications. Figure 1e is a dark-field STEM image in which the bright metal ligaments and dark pores can be observed. Although the atomic-thick graphene cannot be clearly seen in the STEM image, the element mappings (Figure 1f) reveal that a thin carbon layer is uniformly coated on the Ni ligament surface. There is a small amount of oxygen which mainly comes from the oxygen-containing groups on the graphene surface, as demonstrated by X-ray photoelectron spectroscopy (XPS) showing below. Besides Ni, uniformly distributed Mn can also be observed in the metal ligaments, which is the residual Mn from the dealloyed $Ni_{30}Mn_{70}$ precursor according to the EDS analysis (Figure S1a). The water droplet contact angle (Figure S1c) indicates a good wettability of the graphene@np-Ni, which makes it suitable as a water splitting catalyst.

The chemistry of the graphene@np-Ni hybrid was inspected by X-ray photoelectron spectroscopy (XPS). The high-resolution carbon 1s XPS spectrum (Figure S2) shows one main peak at 284.6 eV which corresponds to the graphite-like sp2 carbon, indicating that most C atoms in the graphene layers are arranged in a conjugated honeycomb lattice. A small part of functional groups, such as hydroxyl (C-OH) and carboxyl (C=O) groups, can also be detected[57]. For Ni, the main peak appears at 852.7 eV (Figure 2a), which is in good agreement with the metallic Ni(0) 2p3/2 (852.5-853.0 eV) peak[58, 59]. The peak at ~870.9 eV is assigned to 2p1/2 spin-orbit component of zero-valent metallic Ni. Moreover, a very weak peak at ~856.2 eV, corresponding to oxidized Ni(II), can be seen. The trace-level oxidized Ni(II) may come from incomplete reduction of oxidized np-Ni surface before graphene growth. The oxygen 1s peak at ~531.9 eV, related to Ni hydroxides, shows a very weak signal (Figure 2b), suggesting the low oxidation state of the Ni surface.

Cyclic voltammetry (CV) was used to evaluate the OER activity of the 3D graphene@np-Ni electrode. The performance of the bare np-Ni electrode without graphene was also studied for comparison. For graphene@np-Ni, in the first cycle, no obvious Ni redox peaks are observed, however, significant OER current density still appears after ~1.6 V vs RHE (Figure 3a). As the cycles increase to 10, the weak anodic and cathodic peaks can be observed between 1.2 and 1.4 V, with a peak separation of ~69 mV, corresponding to the $Ni(OH)_2$/NiOOH redox reactions[60]. However, the OER performance is not affected by the formation of Ni (oxy)hydroxides (Figure 3a). In contrast, the bare np-Ni electrode has a large anodic/cathodic peak separation of 103 mV (Figure 3b). The much smaller anodic and cathodic peak separation demonstrates that the graphene@np-Ni electrode facilitates the electrochemical reactions. The two electrodes show the similar onset potential of OER at ~1.530 V (vs RHE) in 1.0 M KOH solution as shown in the enlarged potential-current curves (Figure 3c). When the OER current density reaches 50 mA cm^{-2}, the applied potential is ~1.690 V (overpotential: 460 mV) for the graphene-coated electrode while it is ~1.758 V (overpotential: 528 mV) for the bare np-Ni electrode. When the applied potential increases to 1.823 V, the OER current density of graphene@np-Ni (180 mA cm^{-2}) is more than two times higher than that of the bare np-Ni electrode (76 mA cm^{-2}). Accordingly, graphene@np-Ni gives a much smaller Tafel slope of 45 mV/decade in comparison with the bare np-Ni (77 mV/decade) (inset in Figure 3b). The Tafel slope of graphene@np-Ni is also smaller than reported Co_3O_4/graphene (67 mV/decade)[61] and $NiCo_2O_4$/graphene catalysts (156 mV/decade)[32]. Consequently, the graphene coating significantly enhances the OER activity of np-Ni. Moreover, the overpotential of graphene@np-Ni is only 360 mV at the current density of 10 mA cm^{-2} which is comparable with the state-of-the-art $NiFeO_x$ catalyst (overpotential: ~350 mV)[62]. At 50 mA cm^{-2}, the overpotential is ~460 mV, which is better than or comparable with many recently reported results. A detailed comparison is shown in Table S1. It is worth noting that the OER current and onset potential of graphene@np-Ni do not show noticeable changes with the

increase of scan rates from 5 to 80 mV s^{-1} while the anodic and cathodic peaks of the $Ni(OH)_2$/NiOOH redox reactions strongly depend on scan rates (Figure S3a). The weak rate dependence of graphene@np-Ni may benefit from the highly conductive and bi-continuous porous structure that allows a fast charge and mass transport during the reactions.

The electrochemical stability of the graphene@np-Ni and bare np-Ni electrodes was evaluated by continuous CV cycling in 1.0 M KOH solution at a sweeping rate of 5 mV s^{-1}. With the increase of the cycling number, the two electrodes exhibit enlarged signals and more separated peaks from the redox reactions of $Ni(OH)_2$/NiOOH (Figure 3d and e), indicating the formation of more nickel hydroxide. For the bare np-Ni electrode, the anodic current at 1.823 V decreases obviously (72% of the initial value) together with the increase of the onset potential to ~1.673 V after 400 cycles (Figure 3c and d). In contrast, the 3D graphene@np-Ni electrode even shows a slightly increased anodic current at 1.823 V and, importantly, the onset potential keeps nearly constant after 1000 cycles (Figure 3c and e), demonstrating the significant enhancement in the electrochemical stability of np-Ni based catalysts by the atomically-thick graphene coating, and the weak dependence of the OER activity of graphene@np-Ni on the formation of $Ni(OH)_2$. After cycling, electrochemical impedance spectra (EIS) were investigated. In comparison with that of the bare np-Ni electrode, the EIS spectrum of graphene@np-Ni shows a much small arc in the high frequency region and a larger slope in the low frequency region (Figure 3f), indicating that the graphene@np-Ni electrode has a very low impedance resistance and high efficiency of charge transfer between the catalyst and electrolyte. The increased electrode resistance and activity degradation of the bare np-Ni should be mainly due to the excess formation of Ni hydroxide on the surface of np-Ni. Thus, it is reasonable to deduce that the coated graphene layer protects Ni oxidation and provides an easy path for fast electron transport and rapid interface reactions although more defects can be detected by Raman after long-term cycling (Figure 1c).

XPS analysis was employed to investigate the chemical states of the graphene@np-Ni and bare np-Ni after 100 CV cycles. The graphene@np-Ni electrode shows a main Ni 2p3/2 peak at 855.8 eV, which can be ascribed to $Ni(OH)_2$ and NiOOH[63, 64]. The peak at 852.5 eV is from the metallic Ni(0), indicating the coexistence of Ni hydroxide and pure Ni surface (Figure 2c). Similar to the graphene-coated np-Ni, a Ni^{2+} 2p3/2 peak at 855.4 eV can be observed from the bare np-Ni electrode while the metallic zero-valent Ni cannot be detected (Figure 2e), suggesting that a much thicker hydroxide/oxide layer is formed compared to graphene@np-Ni. In the O 1s peak region (Figure 2d), the graphene@np-Ni electrode only shows one peak at ~531.5 eV which corresponds to the Ni hydroxide[64]. While the bare np-Ni electrode exhibits a predominant peak at ~531 eV and a weak peak at ~529.2 eV, corresponding to the Ni hydroxide and Ni oxide[64, 65], respectively (Figure 2f), suggesting the severe oxidation of Ni surface. According to the XPS results, it can be concluded that the bare np-Ni electrode has been severely oxidized together with dehydrated after anodization while the graphene coating significantly stabilizes the electrode with the formation of much less hydroxide.

The 100-cycled samples were further examined by SEM and TEM. The overall morphology of graphene@np-Ni does not show too much change after the test (Figure 4a) in comparison with the as-prepared one (Figure 1a). The zoom-in SEM image reveals the heterogeneous formation of nano-sized fibrous Ni hydroxide in the regions with a high curvature gradient while the hydroxide cannot be seen in relatively flat regions (Figure 4b), which is in line with the XPS result. In contrast, the bare np-Ni exhibits a much rougher surface covered by a thick layer of Ni hydroxide/oxide (Figure 4c). The observations provide the direct evidence that the atomically thick graphene coating can dramatically stabilize the np-Ni by preventing the oxidation of nanostructured Ni. The bright-field TEM image and selected area electron diffraction further confirm the formation of

fiber-like nanostructured Ni hydroxide that sprouts from the Ni ligaments (Figure 4d and Figure S4). Since atomically thick graphene is an impermeable membrane to any liquid,[66] a perfect graphene coating will not allow ionic trans-diffusion between metallic Ni ligaments and alkaline electrolytes to form Ni hydroxide. As shown in the SEM micrograph (Figure 4b), the fiber-like Ni hydroxide mainly appears in highly curvature regions where graphene often has a high density of topological defects[52] that may allow the slow diffusion of Ni ions to the topmost surface of graphene coating to form the nano-sized Ni hydroxide. Apparently, the resultant ultrafine fiber-like Ni hydroxide is expected to have a high electrocatalytic activity because of a large surface area and close connection with highly conductive graphene coating and Ni substrate. It should be noted that the residual Mn (~10 at.%) is not beneficial for the high OER activity of the graphene@np-Ni (Figure S3b). Considering the synergistic effect by the addition of Fe in Ni-based OER catalysts[62, 67], and the activity could be further enhanced by using NiFe alloys.

Besides the regions with the fiber-like nanostructured Ni hydroxide, we noticed that a large fraction of the 100-cycled graphene@np-Ni sample is actually free of hydroxide/oxide on the top of the graphene coating. Considering that the superior OER activity of graphene@np-Ni starts from the first CV cycle without the formation of detectable Ni hydroxide (Figure 3a), one can deduce that the graphene@np-Ni itself is catalytically active and the atomically thick graphene layer may act as an electron transfer media between under layer Ni and alkaline solutions for catalyzing OER. In fact, the weak dependence of the OER activity of graphene@np-Ni on the formation of $Ni(OH)_2$ during CV cycling also supports the assumption.

To understand the OER activity of the graphene@np-Ni without forming adequate Ni hydroxide, density functional theory (DFT) calculations were performed to predict free energies of the four-electron reaction path on both pristine graphene and graphene@np-Ni. The variation of water splitting reaction is obtained by changing the term eU in the free energy per electron

transferred to the electrodes. Notice that the equilibrium potential is set to be a theoretical value of 1.23V of the water electrolysis. All free energies are calculated at ¼th of monolayer graphene covered with HO, O and HOO, respectively. As shown in Figure 5a and Table S2, the first two reaction steps on the pristine graphene are still endothermic for the equilibrium potential (1.23 V), and that an overpotential of 1.06 V is necessary to make all steps down-hill in the free energy, i.e. at the potential of 2.29 V where the oxygen evolution takes place. A large free energy difference (~1.13 V) is found for the second step, indicating that the O* formation is difficult on the pristine graphene surface and hence low oxygen evolution activity. However, for the graphene@np-Ni, our calculations illustrate that a lower potential of 1.65V is required to make all the free energies downhill (Figure 5b), corresponding to the overpotential of 0.42V, in approximate agreement with the experimental result of ~0.360 V at the current density of 10 mA cm^{-2}. Figure S5 exhibits the similar result when all free energies are calculated at 1/8th of monolayer graphene covered with HO, O and HOO, respectively. Noteworthy, each of the four steps in the reaction nearly has the same change in the free energy, revealing that the graphene@np-Ni itself is a good catalyst for water splitting. To elucidate the physical origins of the high OER activity, the calculated charge density difference is shown in Figure 5c and the density of states are shown in Figure S6. The results indicate that the hybridization between graphene p_z and Ni *3d* states results in new electronic states of carbon atoms locating near the Fermi level, which makes graphene easily absorb HO$^-$ and provides a fast electron transfer path. The DFT calculations are also in line with the previous theoretical prediction that the electron coupling between graphene and the transition metals can significantly enhance the oxygen binding strength of carbon atoms in N-doped graphene supported by Co(111) and Fe(110) substrates.[68]

CONCLUSIONS

We fabricated a robust 3D graphene-coated np-Ni electrode by using a nanoporous Ni-based CVD approach. It was found that the atomically thick graphene coating can significantly improve the catalytic activity and electrochemical stability of Ni. The graphene@np-Ni electrode presents a low OER overpotential of ~360 mV at the current density of 10 mA cm^{-2}, a large OER current density of 180 mA cm^{-2} at 1.823 V and a long cycling lifetime. EIS measurements demonstrate that the free-standing graphene@np-Ni electrode has a very low impedance resistance and high efficiency of charge transfer between the catalyst and electrolyte. Importantly, the high OER activity is achieved from the metallic state of Ni from the hybridized electronic states of graphene p_z and Ni *3d* orbitals. The discovery of the non-oxidation transition metal OER catalyst may paves a new way for designing highly stable, electrically conductive and free-standing catalytic anodes for renewable energy applications.

EXPRIMENTAL METHODS

Materials synthesis. $Ni_{30}Mn_{70}$ alloy sheets with a thickness of 50 μm were prepared by melting pure Ni and Mn (>99.9 at.%) in an Ar-protected arc furnace followed by room-temperature rolling. Nanoporous Ni substrates with a nanopore/ligament size of ~10 nm were prepared by chemically dealloying the $Ni_{30}Mn_{70}$ precursor alloy in a 1.0 M $(NH_4)_2SO_4$ aqueous solution at 50 °C for 12 h.[49] The as-prepared nanoporous Ni was then dried and annealed in a CVD system under mixed atmosphere of H_2, Ar and benzene, at 900 °C for 5 min to fabricate the graphene-protected nanoporous Ni. Bare nanoporous Ni with a similar ligament/pore size was also prepared for comparison by annealing under the same condition without benzene for graphene growth. A Mn-rich (~20 at.%) nanoporous Ni was prepared by dealloying the NiMn alloy under the same conditions with less time (6 h).

Microstructure Characterization. The microstructure of the samples was characterized by a transmission electron microscope (TEM, JEOL JEM-2010F) and a field-emission scanning electron microscope (SEM, JEOL JSM-6700) equipped with an Oxford energy-dispersive X-ray spectrometer (EDS). Raman spectra were recorded in a micro-Raman spectrometer (Renishaw InVia RM 1000) with an incident wavelength of 514.5 nm. XPS analysis was performed by using an X-ray photoelectron spectroscopy (AXIS ultra DLD, Shimazu) with Al *Ka* using X-ray monochromator.

Electrochemical measurements. Electrochemical tests were carried out by using an electrochemical workstation (Iviumstat Technology) in a three-electrode cell with a Pt foil as the counter electrode and Ag/AgCl as the reference electrode. All measurements were conducted under pure O_2 saturation to ensure the O_2/H_2O equilibrium at 1.23 V vs RHE. Linear scan voltammograms and cyclic voltammetry were conducted with a scan rate of 5 mV s^{-1}. Electrical impedance spectroscopy was recorded under the following conditions: ac voltage amplitude 5 mV, frequency ranges 100 to 1 KHz, and open circuit. Tafel plots were obtained at the scan rate of 5 mV s^{-1}. Note that the current density was normalized to the geometrical area and the measured potentials *vs* Ag/AgCl were converted to a reversible hydrogen electrode (RHE) scale according to the Nernst equation ($E_{RHE} = E_{Ag/AgCl} + 0.059\,pH + 0.197$); the overpotential (η) was calculated according to the following formula: $\eta\ (V) = E_{RHE} - 1.23\ V$.

Density functional theory calculations. The most stable top-fcc configuration of the graphene layer on Ni (111) was confirmed and utilized. The first-principles calculations were performed by using the Vienna *ab initio* simulation package (VASP), based on the spin-polarized density functional theory within the generalized gradient approximation (GGA). The electron-ion interactions were presented by the Troullier-Martins-type norm-conserving pseudopotentials with a partial core correction and the GGA exchange-correlation potential in the form of Perdew-Burke-

Ernzerhof (PBE) functional was adopted. A 10 Å of vacuum in the z-direction was used to separate neighboring slabs. In the self-consistent calculations of the charge density a 5×5×1 Monkhorst-Pack *k* grid is employed and we fixed the bottom layer to obtain a better surface relaxation until the Hellmann-Feynman forces are less than 0.01 eV/Å.

The reaction free energy is calculated by:

$$\Delta G(U, pH = 0, T = 298.15\ K) = \Delta G_0 - eU$$

$$\Delta G_0 = \Delta E + \Delta ZPE - T\Delta S,$$

where the binding energy ΔE is calculated as shown below. The binding energy is corrected for the changes in entropy and zero point energy. The binding energies of the intermediates HO*, O* and HOO* on the graphene, Ni, and graphene@np-Ni surfaces were calculated by:

$$\Delta E_{HO^*} = E(HO^*) - E(*) - \left(E_{H_2O} - \frac{1}{2}E_{H_2}\right)$$

$$\Delta E_{O^*} = E(O^*) - E(*) - (E_{H_2O} - E_{H_2})$$

$$\Delta E_{HOO^*} = E(HOO^*) - E(*) - \left(2E_{H_2O} - \frac{3}{2}E_{H_2}\right);$$

in which $E(*)$, $E(HO^*)$, $E(O^*)$ and $E(HOO^*)$ are the ground state energies of the clean surface and the surfaces with HO, O and HOO absorbed, respectively. E_{H_2O} and $E_{H_2}$are the calculated energies of H_2O and H_2 molecules in the gas phase. The * represents active site on the surface.

ACKNOWLEDGEMENTS

This work was sponsored by World Premier International (WPI) Research Center Initiative for Atoms, Molecules and Materials, MEXT, Japan. H.J.Q. is supported by the Japan Society for the

Promotion of Science (JSPS) postdoctoral fellowship program (P12054) and Innovation project of Harbin Institute of Technology. M.C is sponsored by Whiting School of Engineering, Johns Hopkins University and National Science Foundation (NSF DMR-1804320).

Supporting Information Available. Fabrication of nanoporous Ni, DFT calculations of OER reaction potentials and HRTEM characterization are shown in supporting information. This material is available free of charge *via* the Internet.

References

1. Y. Surendranath, M. W. Kanan and D. G. Nocera, *J. Am. Chem. Soc.*, 2010, **132**, 16501-16509.
2. J. Turner, *Nat. Mater.*, 2008, **7**, 770-771.
3. Y. Tan, M. Luo, P. Liu, C. Cheng, J. Han, K. Watanabe and M. Chen, *ACS Appl. Mater. Interfaces*, 2019, **11**, 3880-3888.
4. Z. Jin, J. Lyu, Y.-L. Zhao, H. Li, X. Lin, G. Xie, X. Liu, J.-J. Kai and H.-J. Qiu, *ACS Materials Lett.*, 2020, **2**, 1698-1706.
5. M. G. Walter, E. L. Warren, J. R. McKone, S. W. Boettcher, Q. X. Mi, E. A. Santori and N. S. Lewis, *Chem. Rev.*, 2010, **110**, 6446-6473.
6. Z. Jin, J. Lv, H. Jia, W. Liu, H. Li, Z. Chen, X. Lin, G. Xie, X. Liu, S. Sun, H.-J. Qiu, *Small*, 2019, **15**, 1904180.
7. M.-R. Gao, X. Cao, Q. Gao, Y.-F. Xu, Y.-R. Zheng, J. Jiang and S.-H. Yu, *ACS Nano*, 2014, **8**, 3970-3978.
8. Y. Gorlin, C.-J. Chung, J. D. Benck, D. Nordlund, L. Seitz, T.-C. Weng, D. Sokaras, B. M. Clemens and T. F. Jaramillo, *J. Am. Chem. Soc.*, 2014, **136**, 4920-4926.
9. X. Liu, Z. Chang, L. Luo, T. Xu, X. Lei, J. Liu and X. Sun, *Chem. Mater.*, 2014, **26**, 1889-1895.
10. Y. J. Sun, C. Liu, D. C. Grauer, J. K. Yano, J. R. Long, P. D. Yang and C. J. Chang, *J. Am. Chem. Soc.*, 2013, **135**, 17699-17702.
11. T. Kou, S. Wang and Y. Li, *ACS Materials Lett.*, 2021, **3**, 224-234.
12. N. K. Chaudhari, H. Jin, B. Kim and K. Lee, *Nanoscale*, 2017, **9**, 12231-12247.
13. Z. Shi, X. Wang, J. Ge, C. Liu and W. Xin, *Nanoscale*, 2020, **12**, 13249-13275.
14. W. Cai, H. Yang, J. Zhang, H. C. Chen, H. B. Tao, J. Gao, S. Liu, W. Liu, X. Li and B. Liu, *ACS Materials Lett.*, 2020, **2**, 624-632.
15. Y. Jiang and Y. Lu, *Nanoscale*, 2020, **12**, 9327-9351.
16. T. Grewe, X. H. Deng, C. Weidenthaler, F. Schuth and H. Tuysuz, *Chem. Mater.*, 2013, **25**, 4926-4935.
17. S. Pintado, S. Goberna-Ferron, E. C. Escudero-Adan and J. R. Galan-Mascaros, *J. Am. Chem. Soc.*, 2013, **135**, 13270-13273.
18. J. W. Zhao, Z. X. Shi, C. F. Li, Q. Ren and G. R. Li, *ACS Materials Lett.*, 2021, DOI: 10.1021/acsmaterialslett.1c00018.
19. Y. Jiao, Y. Zheng, M. Jaroniec and S. Z. Qiao, *J. Am. Chem. Soc.*, 2014, **136**, 4394-4403.
20. E. L. Demeter, S. L. Hilburg, N. R. Washburn, T. J. Collins and J. R. Kitchin, *J. Am. Chem. Soc.*, 2014, **136**, 5603-5606.
21. W. D. Chemelewski, H.-C. Lee, J.-F. Lin, A. J. Bard and C. B. Mullins, *J. Am. Chem. Soc.*, 2014, **136**, 2843-2850.
22. X. Xia, L. Wang, N. Sui, V. L. Colvin and W. W. Yu, *Nanoscale*, 2020, **12**, 12249-12262.
23. T. Maiyalagan, K. A. Jarvis, S. Therese, P. J. Ferreira and A. Manthiram, *Nat. Commun.*, 2014, **5**, 3949.
24. H.-J. Qiu, G. Fang, J. Gao, Y. Wen, J. Lv, H. Li, G. Xie, X. Liu and S. Sun, *ACS Materials Lett.*, 2019, **1**, 526-533.
25. I. Roger, M. A. Shipman and M. D. Symes, *Nat. Rev. Chem.*, 2017, **1, 0003.**
26. C. Roy, B. Sebok, S. B. Scott, E. M. Fiordaliso, J. E. Sorensen, A. Bodin, D. B. Trimarco, C. D. Damsgaard, P. C. K. Vesborg, O. Hansen, I. E. L. Stephens, J. Kibsgaard and I. Chorkendorff, *Nat. Catal.*, 2018, **1**, 820-829.
27. A. Bergmann, T. E. Jones, E. M. Moreno, D. Teschner, P. Chernev, M. Gliech, T. Reier, H. Dau and P. Strasser, *Nat. Catal.*, 2018, **1**, 711-719.
28. U. Y. Qazi, C.-Z. Yuan, N. Ullah, Y.-F. Jiang, M. Imran, A. Zeb, S.-J. Zhao, R. Javaid and A.-W. Xu, *ACS Appl. Mater. Interfaces*, 2017, **9**, 28627-28634.
29. M. Gong, Y. G. Li, H. L. Wang, Y. Y. Liang, J. Z. Wu, J. G. Zhou, J. Wang, T. Regier, F. Wei and H. J. Dai, *J. Am. Chem. Soc.*, 2013, **135**, 8452-8455.
30. D. A. Corrigan, *Phys. Rev. Lett.*, 1987, **134**, 377-384.
31. L. Wang and Y. Yamauchi, *J. Am. Chem. Soc.*, 2013, **135**, 16762-16765.

32. S. Chen and S.-Z. Qiao, *ACS Nano*, 2013, **7**, 10190-10196.
33. R. Subbaraman, D. Tripkovic, D. Strmcnik, K. C. Chang, M. Uchimura, A. P. Paulikas, V. Stamenkovic and N. M. Markovic, *Science*, 2011, **334**, 1256-1260.
34. H. C. Chien, W. Y. Cheng, Y. H. Wang, T. Y. Wei and S. Y. Lu, *J. Mater. Chem.*, 2011, **21**, 18180-18182.
35. M. Gao, W. Sheng, Z. Zhuang, Q. Fang, S. Gu, J. Jiang and Y. Yan, *J. Am. Chem. Soc.*, 2014, **136**, 7077-7084.
36. B. Cui, H. Lin, J. B. Li, X. Li, J. Yang and J. Tao, *Adv. Funct. Mater.*, 2008, **18**, 1440-1447.
37. Y. G. Li, P. Hasin and Y. Y. Wu, *Adv. Mater.*, 2010, **22**, 1926.
38. Y.-F. Li and A. Selloni, *ACS Catal.*, 2014, **4**, 1148-1153.
39. D. Pletcher and X. Li, *Int. J. Hydrogen Energy*, 2011, **36**, 15089-15104.
40. B. Zhang, X. L. Zheng, O. Voznyy, R. Comin, M. Bajdich, M. Garcia-Melchor, L. L. Han, J. X. Xu, M. Liu, L. R. Zheng, F. P. G. de Arquer, C. T. Dinh, F. J. Fan, M. J. Yuan, E. Yassitepe, N. Chen, T. Regier, P. F. Liu, Y. H. Li, P. De Luna, A. Janmohamed, H. L. L. Xin, H. G. Yang, A. Vojvodic and E. H. Sargent, *Science*, 2016, **352**, 333-337.
41. J. Suntivich, K. J. May, H. A. Gasteiger, J. B. Goodenough and Y. Shao-Horn, *Science*, 2011, **334**, 1383-1385.
42. L. Trotochaud, J. K. Ranney, K. N. Williams and S. W. Boettcher, *J. Am. Chem. Soc.*, 2012, **134**, 17253-17261.
43. M. J. Kenney, M. Gong, Y. G. Li, J. Z. Wu, J. Feng, M. Lanza and H. J. Dai, *Science*, 2013, **342**, 836-840.
44. B. Zhang, C. Xiao, S. Xie, J. Liang, X. Chen and Y. Tang, *Chem. Mater.*, 2016, **28**, 6934-6941.
45. E. López-Fernández, J. Gil-Rostra, J. P. Espinós, A. R. González-Elipe, A. de Lucas Consuegra and F. Yubero, *ACS Catal.*, 2020, **10**, 6159-6170.
46. F. E. Sarac Oztuna, T. Beyazay and U. Unal, *J. Phys. Chem. C*, 2019, **123**, 28131-28141.
47. F. Song, M. M. Busch, B. Lassalle-Kaiser, C.-S. Hsu, E. Petkucheva, M. Bensimon, H. M. Chen, C. Corminboeuf and X. Hu, *Acs Central Sci.*, 2019, **5**, 558-568.
48. H. Li, Y. Shao, Y. Su, Y. Gao and X. Wang, *Chem. Mater.*, 2016, **28**, 1155-1164.
49. H. J. Qiu, J. L. Kang, P. Liu, A. Hirata, T. Fujita and M. W. Chen, *J. Power Sources*, 2013, **247**, 896-905.
50. B. Zhang, L. Wang, Z. Cao, S. M. Kozlov, F. P. G. de Arquer, C. T. Dinh, J. Li, Z. Y. Wang, X. L. Zheng, L. S. Zhang, Y. Z. Wen, O. Voznyy, R. Comin, P. De Luna, T. Regier, W. L. Bi, E. E. Alp, C. W. Pao, L. R. Zheng, Y. F. Hu, Y. J. Ji, Y. Y. Li, Y. Zhang, L. Cavallo, H. S. Peng and E. H. Sargent, *Nat. Catal.*, 2020, **3**, 985-992.
51. M. Bajdich, M. Garcia-Mota, A. Vojvodic, J. K. Norskov and A. T. Bell, *J. Am. Chem. Soc.*, 2013, **135**, 13521-13530.
52. H.-J. Qiu, L. Y. Chen, Y. Ito, J. L. Kang, X. W. Guo, P. Liu, H. Kashani, A. Hirata, T. Fujita and M. W. Chen, *Nanoscale,* 2016, **8,** 18551-18557.
53. H. J. Qiu, P. Du, K. L. Hu, J. J. Gao, H. L. Li, P. Liu, T. Ina, K. Ohara, Y. Ito and M. W. Chen, *Adv. Mater.*, 2019, **31**, 1900843.
54. Z. P. Chen, W. C. Ren, L. B. Gao, B. L. Liu, S. F. Pei and H. M. Cheng, *Nat. Mater.*, 2011, **10**, 424-428.
55. Y. Zhang, L. Zhang and C. Zhou, *Acc. Chem. Res.*, 2013, **46**, 2329-2339.
56. Z. Jin, J. Yao, C. Kittrell and J. M. Tour, *ACS Nano*, 2011, **5**, 4112-4117.
57. D. C. Wei, Y. Q. Liu, Y. Wang, H. L. Zhang, L. P. Huang and G. Yu, *Nano Lett.*, 2009, **9**, 1752-1758.
58. Y. Goto, K. Taniguchi, T. Omata, S. Otsuka-Yao-Matsuo, N. Ohashi, S. Ueda, H. Yoshikawa, Y. Yamashita, H. Oohashi and K. Kobayashi, *Chem. Mater.*, 2008, **20**, 4156-4160.
59. J. Legrand, A. Taleb, S. Gota, M. J. Guittet and C. Petit, *Langmuir*, 2002, **18**, 4131-4137.
60. J. Ji, L. L. Zhang, H. Ji, Y. Li, X. Zhao, X. Bai, X. Fan, F. Zhang and R. S. Ruoff, *ACS Nano*, 2013, **7**, 6237-6243.
61. Y. Y. Liang, Y. G. Li, H. L. Wang, J. G. Zhou, J. Wang, T. Regier and H. J. Dai, *Nat. Mater.*, 2011, **10**, 780-786.

62. C. C. L. McCrory, S. Jung, J. C. Peters and T. F. Jaramillo, *J. Am. Chem. Soc.*, 2013, **135**, 16977-16987.
63. D. K. Bediako, B. Lassalle-Kaiser, Y. Surendranath, J. Yano, V. K. Yachandra and D. G. Nocera, *J. Am. Chem. Soc.*, 2012, **134**, 6801-6809.
64. I. G. Casella and M. Gatta, *Anal. Chem.*, 2000, **72**, 2969-2975.
65. E. L. Ratcliff, J. Meyer, K. X. Steirer, A. Garcia, J. J. Berry, D. S. Ginley, D. C. Olson, A. Kahn and N. R. Armstrong, *Chem. Mater.*, 2011, **23**, 4988-5000.
66. S. Garaj, W. Hubbard, A. Reina, J. Kong, D. Branton and J. A. Golovchenko, *Nature*, 2010, **467**, 190-U173.
67. L. Trotochaud, S. L. Young, J. K. Ranney and S. W. Boettcher, *J. Am. Chem. Soc.*, 2014, **136**, 6744-6753.
68. S. Zhou, N. S. Liu, Z. Y. Wang and J. J. Zhao, *ACS Appl. Mater. Interfaces*, 2017, **9**, 22578-22587.

Figures and Captions

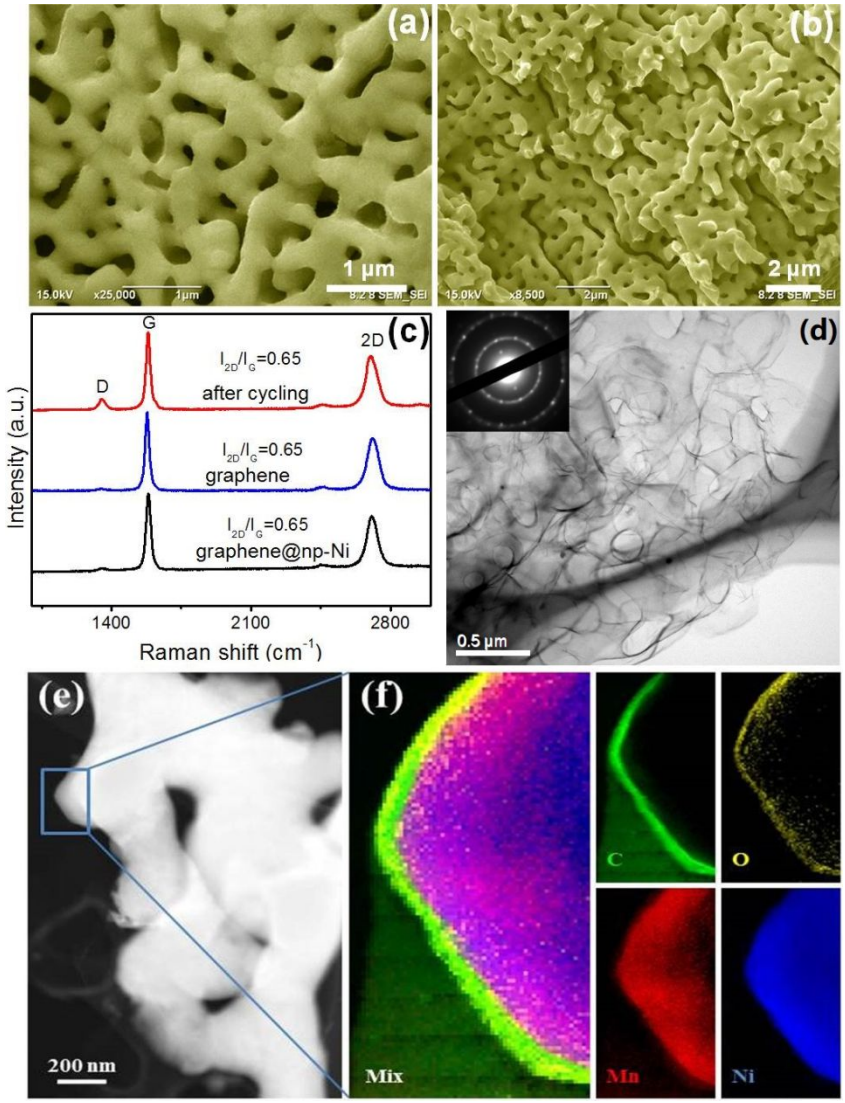

Figure 1. **Microstructure characterization.** SEM images of graphene-coated np-Ni (**a**) plane-view; and (**b**) side-view. (**c**) Raman spectra of the as-grown graphene@np-Ni, pure 3D graphene after the removal of Ni substrate and graphene@np-Ni after 1000 cycles. (**d**) TEM image and electron diffraction pattern (inset) of the nanoporous graphene after the dissolution of np-Ni substrate. (**e**) Dark-field STEM image and (**f**) corresponing element mapping of the 3D graphene@np-Ni.

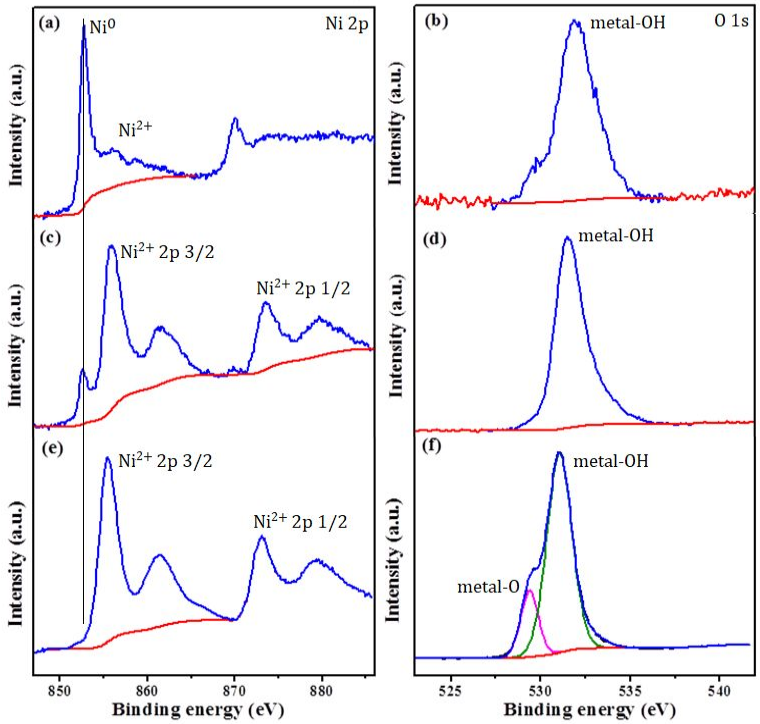

Figure 2. **XPS measurements.** XPS spectra of the as-prepared graphene@np-Ni before (**a**, **b**) and after (**c**, **d**) 100 CV cycles; and the bare np-Ni after 100 cycles (**e**, **f**).

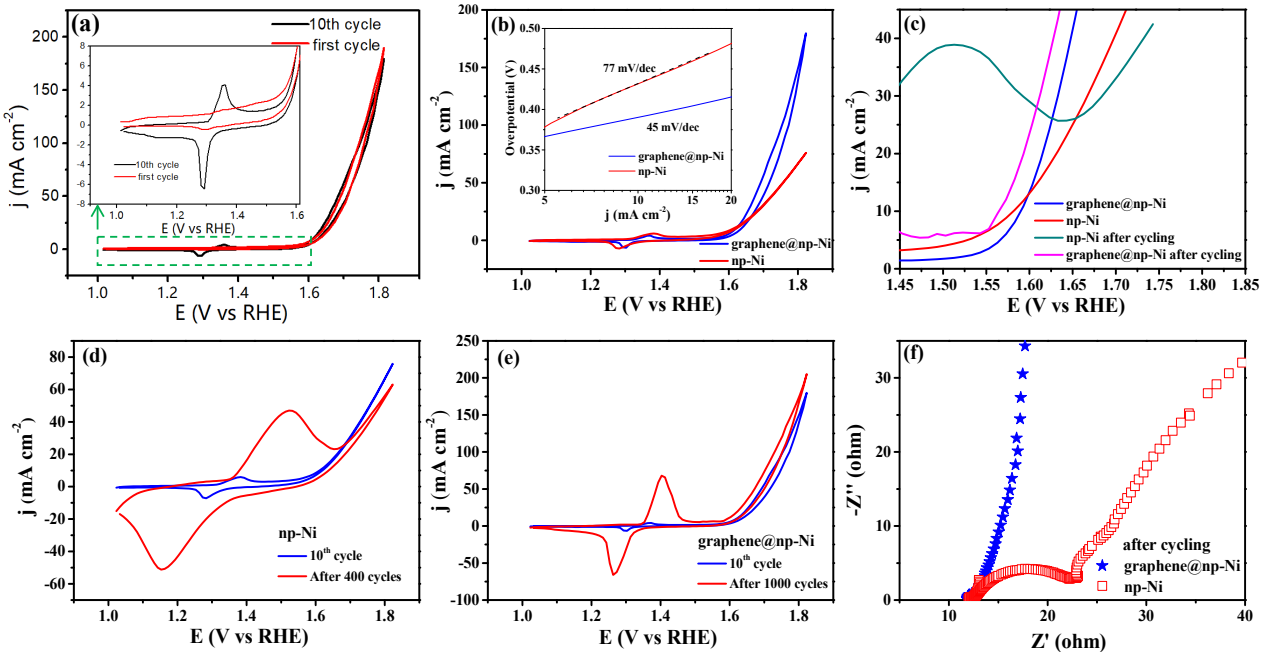

Figure 3. Electrochemical measurements. CV curves of the graphene@np-Ni at first cycle and 10th cycle **(a)**. Inset shows the enlarged curves between 1.0 to 1.6 V. At the first scan, no obvious oxidation peak of Ni can be observed. CV curves showing the redox reactions and oxygen evolutions on graphene@np-Ni (10th cycle) and bare np-Ni electrodes **(b)**. Inset shows the Tafel curves obtained from (b). **P**otential-current curves showing the onset OER potentials of 10th cycled and 1000th cycled graphene@np-Ni and 400th cycled bare np-Ni **(c)**. CV tests revealing the cycling stability of bare np-Ni (**d**) and graphene@np-Ni (**e**) electrodes at a scan rate of 5 mV s^{-1}. Impedance spectra of the graphene@np-Ni after 1000 cycles and bare np-Ni after 400 cycles **(f)**.The electrolyte is 1.0 M KOH aqueous solution.

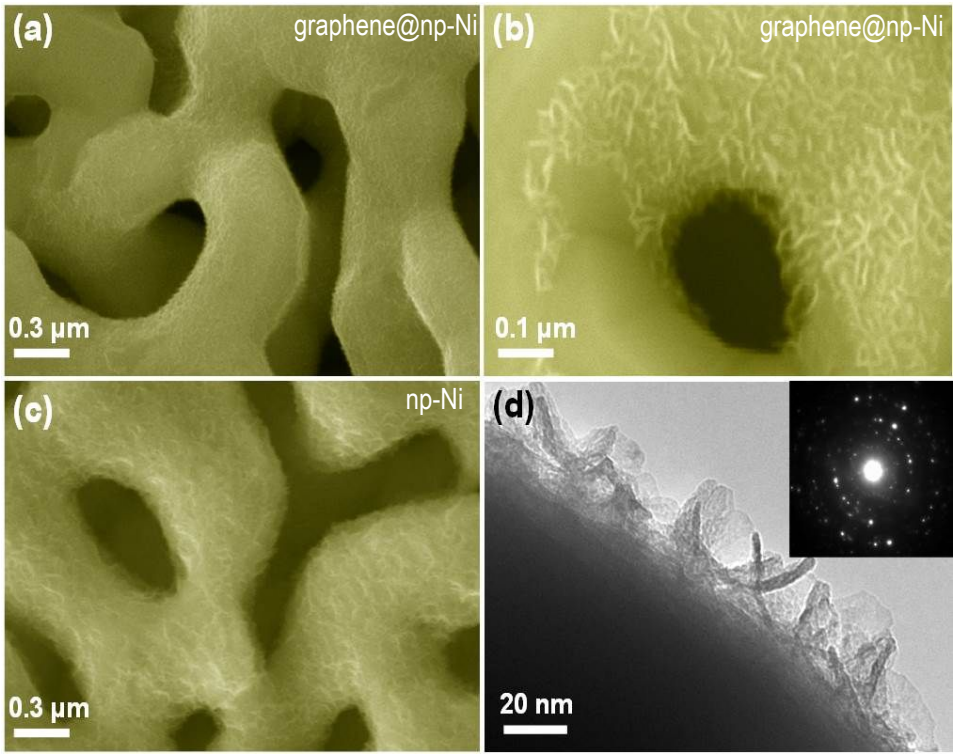

Figure 4. Microstructure characterization after cycling test. SEM images of (**a**, **b**) graphene@np-Ni and (**c**) bare np-Ni after 100 cycles, (**d**) TEM images and electron diffraction pattern (inset) of the grown nickel hydroxides on graphene@np-Ni after 100 cycles.

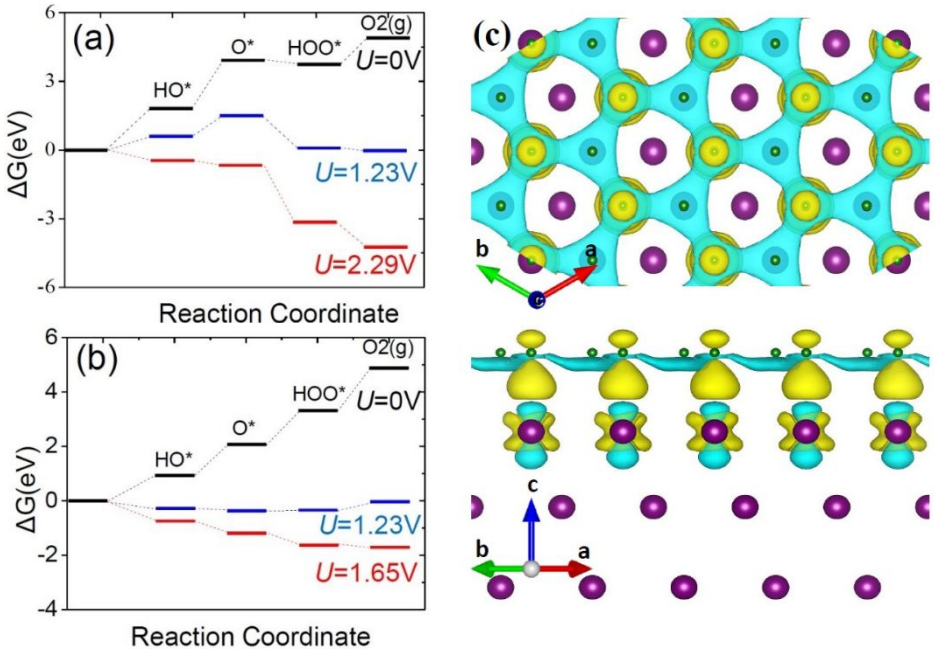

Figure 5. Density functional theory calculations of OER on graphene and graphene@np-Ni. OER on the surfaces of (**a**) pristine graphene; and (**b**) graphene@np-Ni at the different potentials. The variation is obtained by changing the term eU in the free energy per electron transferred to the electrode. Note that the equilibrium potential is set to be a theoretical value of 1.23V. All free energies are calculated at $1/4^{th}$ of a monolayer graphene coverage of intermediates HO, O and HOO, respectively. (**c**) Charge density difference of the graphene@np-Ni system: $\Delta\rho$ = ρ[graphene@Ni(111)] - ρ(graphene) - ρ[Ni(111)]. Top view (top) and side view (bottom); green and purple balls denote C and Ni ions, respectively. Yellow and cyan iso-surfaces correspond to positive and negative values, respectively.